

Can non-propagating hydrodynamic solitons be forced to move?

L. Gordillo^{1,a}, T. Sauma¹, Y. Zárate¹, I. Espinoza², M.G. Clerc¹, and N. Mujica¹

¹ Departamento de Física, FCFM, Universidad de Chile, Casilla 487-3, Santiago, Chile

² Departamento de Física, Pontificia Universidad Católica de Chile, Av. Vicuña Mackenna 4860, Santiago, Chile

Received 1st June 2010 / Received in final form 15 October 2010

Published online 17 December 2010 – © EDP Sciences, Società Italiana di Fisica, Springer-Verlag 2010

Abstract. Development of technologies based on localized states depends on our ability to manipulate and control these nonlinear structures. In order to achieve this, the interactions between localized states and control tools should be well modelled and understood. We present a theoretical and experimental study for handling non-propagating hydrodynamic solitons in a vertically driven rectangular water basin, based on the inclination of the system. Experiments show that tilting the basin induces non-propagating solitons to drift towards an equilibrium position through a relaxation process. Our theoretical approach is derived from the parametrically driven damped nonlinear Schrödinger equation which models the system. The basin tilting effect is modelled by promoting the parameters that characterize the system, e.g. dissipation, forcing and frequency detuning, as space dependent functions. A motion law for these hydrodynamic solitons can be deduced from these assumptions. The model equation, which includes a constant speed and a linear relaxation term, nicely reproduces the motion observed experimentally.

1 Introduction

During the last years, emerging macroscopic particle-type solutions or localized states in macroscopic extended dissipative systems have been observed in different fields, such as: domains in magnetic materials, chiral bubbles in liquid crystals, current filaments in gas discharge, spots in chemical reactions, localized states in fluid surface waves, oscillons in granular media, isolated states in thermal convection, solitary waves in nonlinear optics, just to mention a few. The variety of this type of phenomena evidences the universality of these particle-type solutions. Although these states are spatially extended, they exhibit properties typically associated with particles. Consequently, one can characterize them with a family of continuous parameters such as position, amplitude and width. Hence, these coherent states are particle-type solutions. This is exactly the type of description and strategy used in fundamental physical theories like quantum mechanics and particle physics. Indeed, localized states emerging in extended dissipative systems are composed by a large number of atoms or molecules (of the order of Avogadro's number) that behave coherently. The paradigmatic example of a macroscopic localized state is the existence of solitons, as those reported in fluid dynamics, nonlinear optics and Hamiltonian systems [1]. These solitons arise from a robust balance between dispersion and nonlinearity. The generalization of this concept to dissipative and out of

equilibrium systems has led to several studies in the last decades, in particular to the definition of *localized structures* intended as patterns appearing in a restricted region of space [2,3].

In one-dimensional spatial systems, an adequate geometrical theoretical description of localized states has been established based on spatial trajectories connecting a steady state with itself. They arise as homoclinic orbits from the viewpoint of dynamical systems theory (see the review [4] and references therein), while domain walls or fronts are seen as spatial trajectories joining two different steady states – heteroclinic curves – of the corresponding spatial dynamical system [5]. Localized patterns can be understood as homoclinic orbits in the Poincaré section of the corresponding spatial-reversible dynamical system [4–7]. They can also be understood as a consequence of the front interaction with oscillatory tails [8,9]. There is another type of stabilization mechanism that generates localized structures without oscillatory tails based on non-variational effects [10,11], where front interaction is led by the non-variational terms [12].

Quasi-reversible systems¹ are the natural theoretical framework in which one expects to observe localized structures. Time-reversible and Hamiltonian systems exhibit a family of localized states described by a set of continuous parameters [1]. Thus, when one considers energy injection and dissipation, only few or none solutions of the

^a e-mail: l.jgordillo@gmail.com

¹ Time-reversible systems subjected to small injection and dissipation of energy [13–17].

family survive. The prototype model that presents localized structures or dissipative solitons in quasi-reversible systems is the parametrically driven damped nonlinear Schrödinger equation [18]. This model has been derived in several contexts to describe patterns and localized structures, such as vertically oscillating layer of water [19–21], nonlinear lattices [22], optical fibers [23], Kerr type optical parametric oscillators [24], magnetization in an easy-plane ferromagnetic exposed to an oscillatory magnetic field [25–28], and parametrically driven damped chain of pendula [29,30].

In the last two decades, the properties and mechanisms of creation of localized structures have been established as well as their interactions. However, few studies have been focused on manipulation and control of these coherent states. In the pioneering work of Wu et al. [32], the authors mention that hydrodynamic non-propagating solitons are sensitive to depth gradients. They found that solitons move toward less deep regions with an average velocity of 0.05 cm/s for a 3° tilt angle. This fact suggests that tilting the basin can be used as a spatial control tool, as it induces motion of solitons. A quantitative detailed study of the dynamics of the soliton needs to be performed in order to achieve this. Recent efforts have been accomplished in the context of optical cavities in semiconductors [31], through the use of a phase gradient which induces a drift of cavity solitons.

The aim of this manuscript is to characterize theoretically and experimentally a method of manipulation and control of non-propagating hydrodynamic solitons in a vertically driven rectangular water container based. More precisely, this control is attained by tilting the bottom surface normal with respect to gravity. Close to the Faraday instability, the parametrically driven damped nonlinear Schrödinger equation models this system. The effect of the container inclination is incorporated into the amplitude equation through space-dependent dissipation, injection and detuning. Considering that the tilt angle is small, we deduce an equation for the position of non-propagating hydrodynamic solitons. This equation is characterized by two terms: a constant speed and a linear relaxation process. Therefore, at a given inclination of the cell, the dissipative soliton travels to an equilibrium position through a relaxation process. In the case that the inhomogeneous injection and dissipation of energy are of the same order, the dominant mechanism in the propulsion of dissipative solitons is governed by the inhomogeneous detuning. Experimentally, we have found good agreement with the proposed dynamics of dissipative hydrodynamic solitons under the influence of tilt angle.

The manuscript is organized as follows: the description of the experimental setup and the procedures used in the characterization of the dynamics of dissipative solitons in a tilted cell are presented in Section 2. The theoretical description of the basin subjected to vertical oscillations and deduction of the equation for the position of dissipative solitons under the influence of an inclination is presented in Section 3. Finally, the conclusions are presented in Section 4.

2 Motion of non-propagating hydrodynamic soliton in tilted container

Non-propagating hydrodynamic solitons arise when a quasi 1-D rectangular basin filled with water is excited vertically at certain range of frequencies and amplitudes [32]. These localized states have a subharmonic nature depicted by oscillations at half the forcing frequency. They appear as localized transverse *sloshing* structures on the free surface. The dissipative solitons nucleate from disturbances of the stable flat state. In practice, they can be created by perturbing the water surface with a paddle in such a way that the swaying resembles solitons typical *sloshing* motion.

2.1 Experimental setup and procedure

The experiments are done with a rectangular plexiglas basin, $L_x = 50.0$ cm long, $L_y = 2.54$ cm wide and $L_z = 10.0$ cm high. The cell was carefully machined on a plexiglas block to ensure parallelism of lateral walls. The basin is filled up to $H = 2$ cm in depth with a mixture of 252 cm³ of water, 2 cm³ of Kodak Photo Flo® 200² and some drops of black ink. The mixture is prepared a day before measurements are done. Free surface saturation with contaminants plays an important role for reproducibility [33].

The cell is driven sinusoidally by an electromechanical shaker lying on a three-point leveling system which allows longitudinal tilting (see Fig. 1). The tilt angle ϕ is considered positive for a counter-clockwise rotation of the cell with respect to the horizontal when visualized from the front. The shaker is fed with an amplified sinewave signal generated by a function/arbitrary waveform generator and a power amplifier. Thus, the cell vibration is along the axis of the shaker, with form $y(t) = A \sin(\omega t)$. Solitons can exist at frequencies $f = \omega/2\pi$ slightly below 11 Hz, and normalized accelerations $\Gamma = A\omega^2/g$ around 0.15. The basin acceleration is measured using a piezoelectric accelerometer attached to its bottom surface. It is connected to a signal conditioner, from which the acceleration signal is measured by a lock-in amplifier synchronized with the forcing signal (see Fig. 2a). Acceleration values are provided with precision of 0.001 g. An analog tilt sensor is also placed on the external bottom of the basin. This MEM device is connected to an analog/digital converter which measures angle values within an error of 0.01°.

Two different types of measurements are made on the free surface. Sequences of images taken with a high speed camera provide spatial measurements. On the other hand, local measurements are done using the phase fluctuations of the output signal of a resonant capacitive device.

² This chemical product creates a film which improves significantly wetting at the walls.

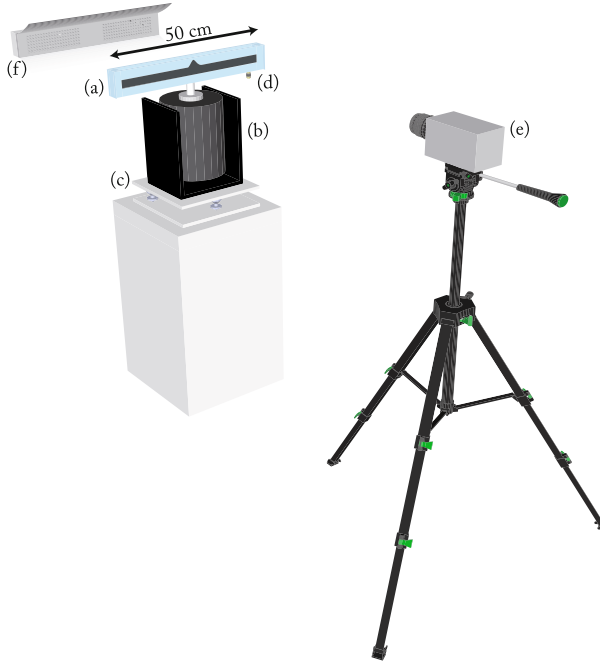


Fig. 1. (Color online) The basin filled with a dyed mixture of water and Kodak Photo Flo (a) is vibrated vertically by an electromechanical shaker. (b). The tilt angle ϕ can be controlled using a three-point level system. Positive ϕ means counter-clockwise rotation of the cell with respect to the horizontal when visualized from the front (c). Acceleration is measured using an accelerometer (d). A high speed camera (e) acquires images of the fluid illuminated from behind by an array of LED lamps (f).

2.1.1 Profile extraction from images

Figure 2a shows the general scheme of the devices involved in the image acquisition process. The basin is illuminated from behind with a LED array as it is shown in Figure 1. This allows a good contrast between the dyed mixture and the white background in the images. Imaging can also be synchronized with an external signal so stroboscopic sequences can be acquired. When this is done, the phase between the forcing and the camera sync signal is fixed in such a way that the soliton seems to be steady at its maximum.

A Matlab program that uses an adaptive threshold finder³ detects the contact line between the free surface and the frontal wall from greyscale images. To increase vertical resolution, the algorithm interpolates the vertical position in the grey level domain to match a local threshold.

2.1.2 Local capacitive measurements

When an insulated thin wire is immersed in a conducting fluid, it behaves as an electrical cylindrical capacitor. The

capacity is proportional to the length of the fluid coating the wire. By means of this, a fixed wire can provide measurements of the fluid level at a single point of the horizontal domain.

Capacity fluctuations can be obtained by connecting the device to a RLC forced circuit (cf. Fig. 2b). When the fluid is in equilibrium, the frequency of the input signal can be tuned up into resonance, typically $f_{RLC} \approx 70$ kHz. At this point, the phase on the resistance voltage becomes linear to capacity variations. High sensitive response in the phase can be attained by choosing properly the circuit elements. In order to measure phase fluctuations, the output signal is connected to a Lock-In amplifier which is synchronized with the RLC circuit forcing input signal (see Fig. 2b).

2.2 Experimental results

We report measurements performed at a fixed vibration frequency $f = 10.4$ Hz and acceleration amplitudes around $\Gamma = 0.1$, region in which the existence and features of non-propagating hydrodynamic solitons have been studied in detail [21]. Typical tilt angles ϕ are between $\pm 1^\circ$.

2.2.1 Spatio-temporal diagrams

Figures 3a and 3b show spatio-temporal diagrams for two different solitons with different time scales and tilt angles. Contact line profiles are extracted using the procedure explained in 2.1.1 and plotted against time.

In Figure 3a, a soliton stands at a fixed position on the center of the basin. Here, $\phi = 0$ and $\Gamma = 0.088$. The camera acquisition rate is 400 Hz, so the soliton fast *sloshing* motion can be observed. However, motion beneath the water baseline cannot be detected as no contrast is available. Thus, the contact lines at the front and rear walls switch on the image at each half cycle.

Figure 3b shows a long-time acquisition for $\phi = -0.42^\circ$ and $\Gamma = 0.110$. The soliton was created at $t = 0$ and images were taken stroboscopically at a fixed rate of 650 mHz. The diagram shows the motion of the particle-type solution, in this case toward shallower regions. These dissipative solitons can be attracted to lateral boundaries and even pinned on them depending on the driving amplitude and frequency [34]. In this study, solitons remain far enough from lateral walls as they move across the principal axis. Lateral boundary effects are negligible if a soliton is a few centimeters apart from the wall.

The trajectories of the dissipative solitons reveal non-trivial time dependence. At a first stage, the center of the solution attains rapidly a constant speed. Wu et al. referred to this short-time scale stage in their work [32]. At a long-time scale stage, solitons converge to a fixed position rather than to a constant velocity as is clearly illustrated in Figure 3b.

Long-time acquisitions were strongly motivated by the fact that the initial velocity for short-time acquisition depends on the locus where the soliton is created. The break

³ By adaptive, we mean that background light local mean value is used for determining a local threshold.

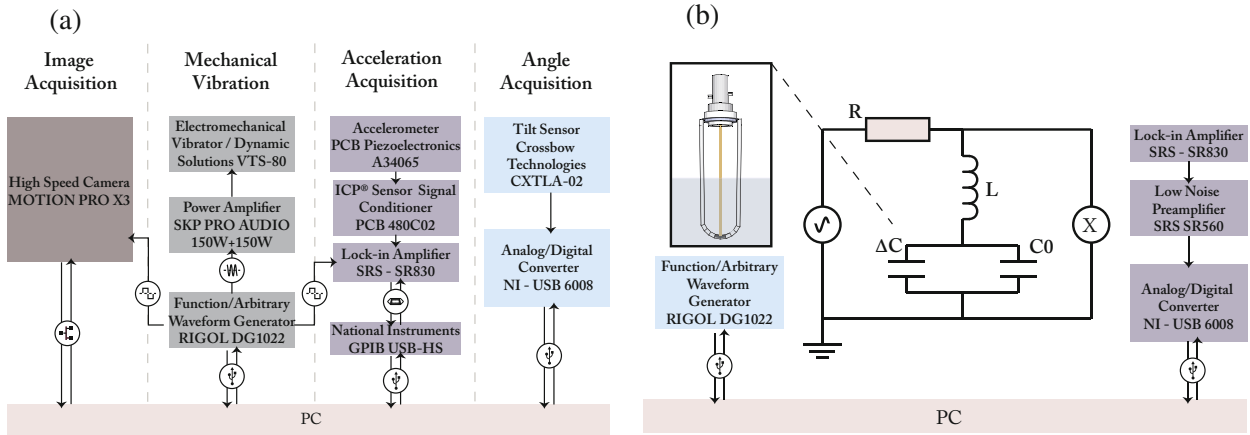


Fig. 2. (Color online) (a) The scheme shows the measurement procedures used for spatial acquisitions. (b) Local acquisitions scheme. The capacitor ΔC represents capacity fluctuations and can be negative. C_0 represents parasitic and zero-level capacity.

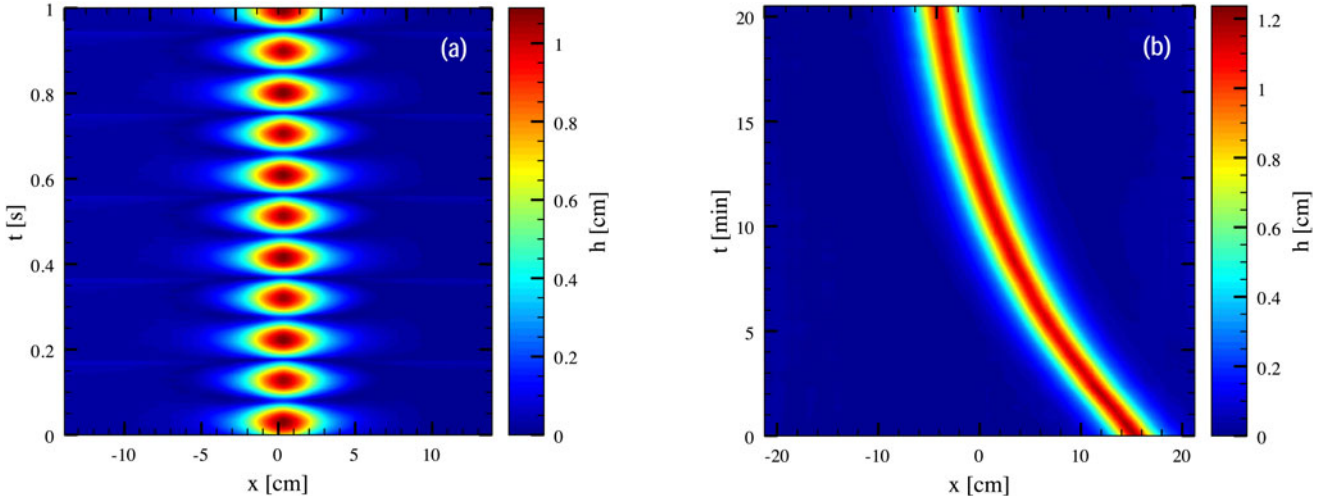


Fig. 3. (Color online) Spatio-temporal diagrams for solitons at different timescales. (a) A soliton *sloshes* back and forth with half the driven frequency, at $\Gamma = 0.088$ and $\phi = 0$. (b) A soliton travels to a shallower region for $\phi = -0.42^\circ$ (clockwise rotation). Here, $f = 10.4$ Hz and $\Gamma = 0.110$. Images are taken stroboscopically when the soliton reaches its maximum after every eight cycles.

of translational symmetry suggests that the speed does not depend only on the depth gradient but also on the local depth.

2.2.2 Velocity vs. position

Soliton dynamics on tilted basins can be well understood by means of the velocity versus position plane. Figure 4a shows *phase plane tracks* for different solitons at different angles. Time series were run twice for each angle to check experimental reproducibility.

For each image sequence, the contact line profile is fitted using the 4-parameters function predicted by theory: $h(x) = A_s \operatorname{sech}[(x - x_o)/w] + h_0$ (see Sect. 3.1, Fig. 8 and Ref. [21]). The positions x_o plotted in Figure 4a are obtained from the parameter which represents the position at which maximum height takes place. Velocities, on the

other axis, are evaluated by differentiating smoothed position data with respect to time.

From the results obtained in the central area of the cell – where edge effects are negligible – the diagram shows that solitons are governed by the simple motion law (cf. Fig. 4a)

$$\dot{x}_0 = -\frac{1}{\tau(\phi)} [x_0 - P(\phi)], \quad (1)$$

where x_0 stands for the position of the maximum of the dissipative soliton, ϕ is the tilt angle of the basin, τ accounts for a relaxation time which characterizes the dynamics of x_0 , P/τ is a characteristic speed of propagation and P is the equilibrium position towards which the dissipative soliton converges.

The model (1) is invariant under spatial and time translations as expected. Lateral boundary effects appear as a change in the slope for positions above $|x_0| = 15$ cm (see Fig. 4a). This equation implies that solitons are

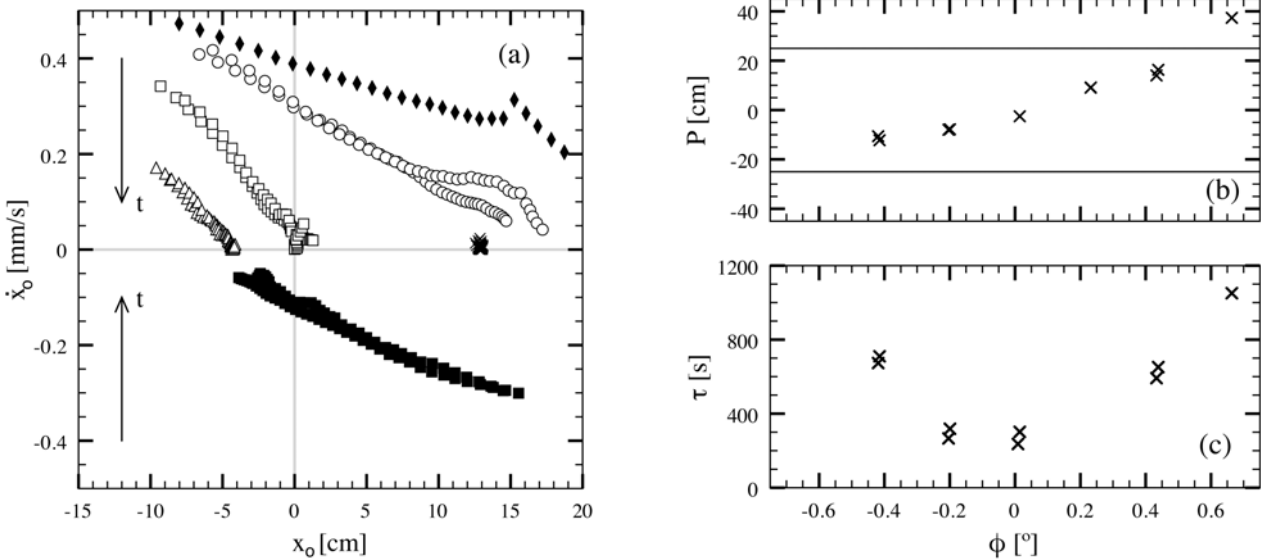


Fig. 4. (a) Soliton velocity \dot{x}_o versus positon x_o plots for different tilt angles ϕ : -0.42° (\blacksquare), -0.20° (\triangle), -0.01° (\square), 0.23° (\times), 0.43° (\circ), 0.66° (\diamond) at constant vertical $\Gamma = 0.131$. The arrows show time direction in the series of points. Solitons can propagate upward (\circ, \diamond), downward ($\triangle, \square, \blacksquare$), or even stay at their position (\times), depending on their initial position with respect to equilibrium. Two experiments are shown for each angle except for $\phi = -0.66^\circ$ (\diamond). (b) Equilibrium position versus tilt angle. P is located in shallower regions as ϕ increases. For $\phi = -0.66^\circ$ (\diamond), the equilibrium position is *virtually* located beyond the basin edge (indicated by horizontal solid lines). (c) Position decay time τ dependence on ϕ . As ϕ increases, convergence to equilibrium position becomes slower. In (b) and (c) errorbars of each realization, obtained by confidence values of fitted parameters, are smaller than symbol size. The scatter of two data points for each angle show that the final errors due to reproducibility are of order of the symbol size.

attracted to an equilibrium position $P(\phi)$ following an exponential law.

Both the equilibrium position P and the exponential decay time τ depend on ϕ . As the tilt angle increases, the equilibrium position is pulled out from the center of the basin even surpassing the basin boundaries. Figure 4a shows phase-space tracks on which solitons get pinned at their equilibrium positions after moving *upward*⁴ or *downward*, respectively. Angle dependence of these two parameters is shown in Figure 4b. Note that the decay time τ is larger for larger angles. Dependence on the angle is plotted in Figure 4c.

2.2.3 Local shape

Solitons amplitude is very sensitive to the fluid depth in homogeneous layers ($\phi = 0$) as it is shown in Figure 5a (symbol \blacksquare).

When the basin is tilted, traveling solitons change as they move across the basin. Their amplitude decrease as they move to their equilibrium position. Two cases can be well identified depending on the tilt angle.

When the skew angle is higher than 1° so the equilibrium position is beyond lateral boundaries, the amplitude variations can be understood in terms of the local mean depth as it is shown in Figure 5 (symbols $\square, \triangle, \circ, \diamond$).

By contrast, when the tilt angle is small enough to allow equilibrium inside the boundaries (symbol $+$), the

amplitude dependence becomes non trivial. Solitons still decrease their amplitude as they move but dependence with local mean depth is not monotonic. Amplitude minimum occurs very close to equilibrium position.

Figure 6 shows soliton local mean phase θ as function of position for two tilt angles, $\phi = -2^\circ$ and $\phi = 2^\circ$. To measure θ , we obtain the maximum soliton height as a function of time $A_s(x_o, t)$ for two periods of oscillation while the soliton moves across the basin. This function is then fitted to $A_s(x_0)|\cos(\omega t + \theta)|$ for different soliton positions across the cell. Despite the large errorbars, a weak spatial dependence of θ is observed. Theoretically, local phase is related to the ratio μ/γ (see 3.1). The weak dependence of θ on x is consistent with the weak dissipation space dependence that will be presented below. However, a spatial dependence of γ can not be discarded completely.

2.2.4 Soliton parameters and physical quantities

Results have shown that solitons parameters: amplitude and phase have different behaviors when the soliton propagates. Amplitude variations are important while phase remains almost constant when the soliton moves. One is tempted to ask how physical quantities as dissipation rate and detuning are related to these parameters when motion occurs.

Soliton damping rate depends mainly on three mechanisms: viscous effects in the boundary layers at walls, at the free surface and capillary hysteresis at the contact

⁴ We define *upward* direction against depth gradient.

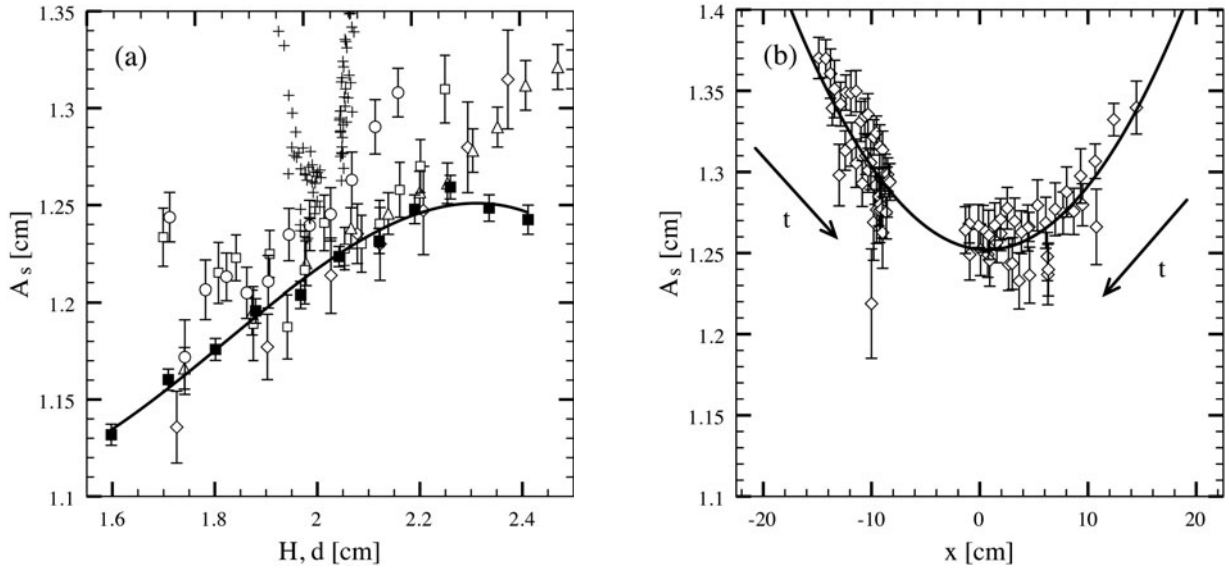


Fig. 5. (a) Soliton amplitude A_s versus fluid depth H for a homogeneous fluid layer ($\blacksquare, \phi = 0^\circ$). In addition, A_s versus the soliton local mean depth d (at each position as it moves toward its equilibrium) is plotted for different ϕ : -2.0° (\triangle), -1.0° (\square), 0.3° (+), 1° (\circ) and $+2^\circ$ (\diamond). Errorbars for $\phi = 0.3^\circ$ are shown in (b). In all the tilted cases, the solitons equilibrium positions are located beyond domain boundaries, except for $\phi = 0.3^\circ$. For all cases $f = 10.4$ Hz and $\Gamma = 0.117$. (b) Soliton amplitude versus position for $\phi = 0.3^\circ$. Here, the equilibrium position lies inside the basin. Consequently, A_s develops a minimum. Arrows indicate the time direction for each data set. Here, $f = 10.4$ Hz and $\Gamma = 0.121$. In both figures, solid lines are guides to the eye.

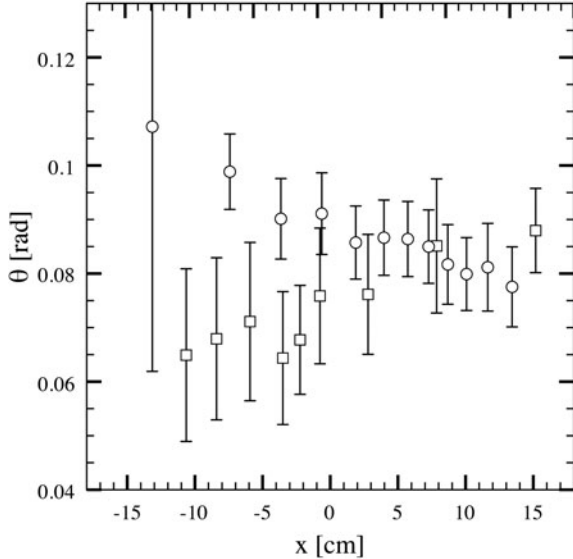


Fig. 6. Soliton local mean phase θ as function of position x for $\phi = -2^\circ$ (\circ) and $\phi = 2^\circ$ (\square) for $\Gamma = 0.118$. Errorbars are computed from confidence values of fitted parameters.

lines [33]. As water depth changes along the basin, dissipation may become non uniform as well.

To measure how dissipation changes along the basin for a fixed angle, local capacitive measurements are performed with the soliton placed at several positions. When the soliton is close enough to the capacitive sensor, the vibration of the basin is interrupted. The soliton amplitude decays exponentially to the flat state. The damping rate

is obtained by applying linear fits to data on the semilog plane. Figure 7a shows the damping factor for different positions with $\phi = -0.9^\circ$. Similar data have been obtained for the pattern state, Faraday waves, which coexists in the same region of parameters.

Experimental measurements of the soliton decay rates show high variance. This is due to the lack of a large enough separation of timescales of the different modes. Oscillation rate is just five times larger than the damping rate. In spite of this, Figure 7a shows that the damping rate for solitons is sensitive to tilting and has a tendency to decrease towards shallower water, at least more than Faraday waves damping rate.

The fact that damping rate (and dissipation) increases for increasing depth is consistent with Miles [33] dissipation estimations for homogeneous layers. His theoretical estimations for the three mechanisms point to different height dependences for each one of them: damping rate of viscous effects at the walls first decreases as function of H and then increases after a characteristic length; surface damping rate is a decreasing function of H ; finally, the contact line damping rate increases as function of H . Our results indicate that probably the first and third mechanisms are dominant. Miles also stresses the fact that the basin wall polishing has a strong effect on dissipation, which could explain the large scatter of damping rates across the cell and the correlation between lower and larger damping rates for solitons and Faraday waves.

Detuning is related with the forcing frequency and the natural frequency of the first transverse mode which supports the soliton. As this natural frequency depends on the fluid depth (see [33]), detuning may change across

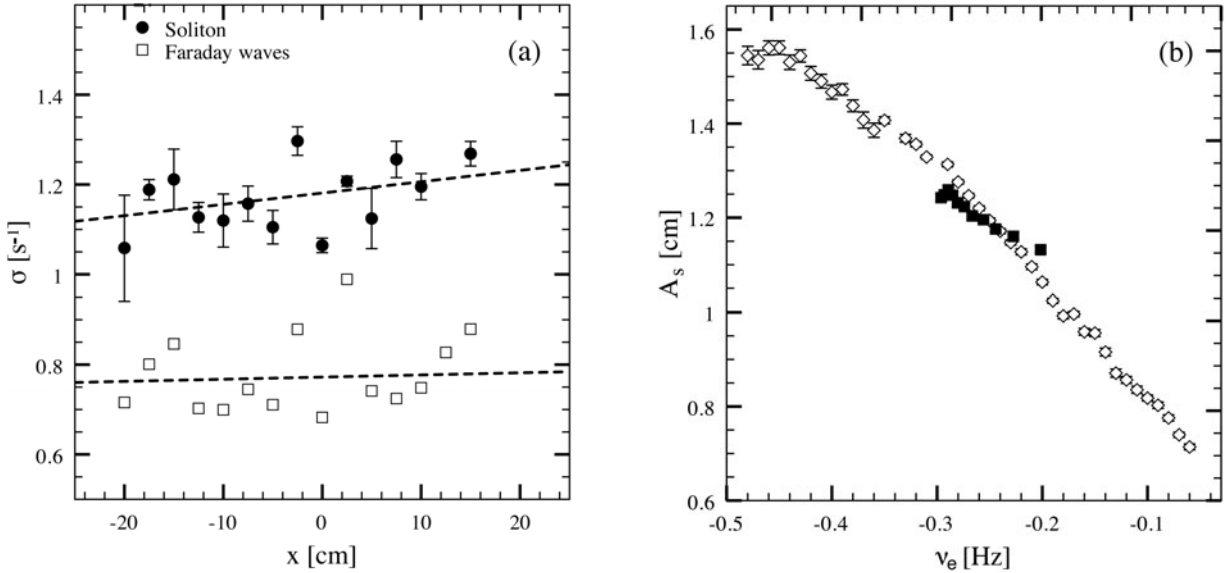


Fig. 7. (a) Amplitude damping rate versus position for Faraday waves (\square) and dissipative solitons (\bullet) for $\phi = -0.9^\circ$ and $\Gamma = 0.111$. Errorbars of soliton data are obtained from statistics of four acquisitions. Faraday waves damping rates were measured once. Solitons decay rate dependence on ϕ seems to be asymmetrical revealing non-homogeneity along the principal axis of the basin. (b) Soliton amplitude versus experimental detuning $\nu_e = f/2 - f_o$ for $\phi = 0^\circ$. Open symbols (\diamond) correspond to variations of forcing frequency f [$\nu_e = \nu_e(f)$]; solid symbols (\blacksquare) correspond to variations of fluid depth H [$\nu_e = \nu_e(H)$]. In the first case, $\Gamma = 0.125$, whereas for the second case, $\Gamma = 0.117$. The plot shows high sensitivity of A_s to detuning parameter ν_e .

the basin too. Detuning measurements are not performed directly. Instead, amplitude sensitivity to detuning parameter is measured.

Figure 7b presents the amplitude dependence on the experimental detuning $\nu_e = f/2 - f_o$ for an homogeneous layer at a fixed forcing amplitude. Here, f_o is the natural frequency of the first transverse mode ($f_o = 5.47$ Hz for $H = 2$ cm). f_o depends on the basin's geometry and layer depth H through the gravity wave dispersion relation

$$\omega_o^2 = gk \tanh(kH), \quad (2)$$

where $\omega_o = 2\pi f_o$. Thus, ν_e can be controlled by variation of f or H (symbols \diamond and \blacksquare respectively). In Figure 7b, the data obtained by varying H are the same as those presented in Figure 5a (\blacksquare). The agreement with the data obtained by changing f is quite good.

The importance of these physical quantities will be discussed in Section 4.

3 Theoretical description

The dynamics of a layer of incompressible fluid that is driven by a sinusoidal force with frequency Ω normal to the free surface is modeled by the dimensionless parametrically driven and damped nonlinear Schrödinger equation [19,20]

$$\partial_t \psi = -i\nu\psi - i|\psi|^2\psi - i\partial_{xx}\psi - \mu\psi + \gamma\bar{\psi}, \quad (3)$$

where the order of parameter $\psi(x, t)$ is a one dimensional complex field, and $\bar{\psi}$ stands for the complex conjugate

of ψ . The surface displacement from flat interface $h(x, t)$ and the velocity potential at the free surface $\phi(x, t)$ are slave variables which are of the form $h = \psi e^{-i\Omega t/2} + c.c.$ and $\phi(x, t) = -i\psi e^{-i\Omega t/2} + c.c.$, respectively (see [20] and references therein). The detuning parameter is ν , which is proportional to the difference between $\Omega/2$ and the resonant standing wave angular frequency. The damping parameter is μ , which is proportional to the kinematic viscosity of the fluid, which accounts for the dissipation mechanisms of the system and γ is the forcing acceleration amplitude. For $\mu = \gamma = 0$, equation (3) becomes the well-known nonlinear Schrödinger equation [1], which describes the envelope of an oscillatory system. This model is a time reversal Hamiltonian system with the transformation $\{t \rightarrow -t, \psi \rightarrow \bar{\psi}\}$. The terms proportional to μ and γ break the time reversal symmetry, and represent energy dissipation and injection, respectively. The higher-order terms in equation (3) are ruled out by a scaling analysis, since $\mu \ll 1$, $\nu \sim \mu \sim \gamma$, $|\psi| \sim \mu^{1/2}$, $\partial_x \sim \mu^{1/2}$, and $\partial_t \sim \mu^{1/2}$.

3.1 Dissipative solitons

A trivial state of equation (3) is the homogeneous state $\psi_0 = 0$, which represents the flat or quiescent solution of the fluid layer. For negative ν , the parametrically driven damped nonlinear Schrödinger equation exhibits localized states supported asymptotically by the quiescent state. In order to obtain these localized states we use the transformation $\psi(x, t) = R(x, t)e^{i\theta(x, t)}$. Then the parametrically

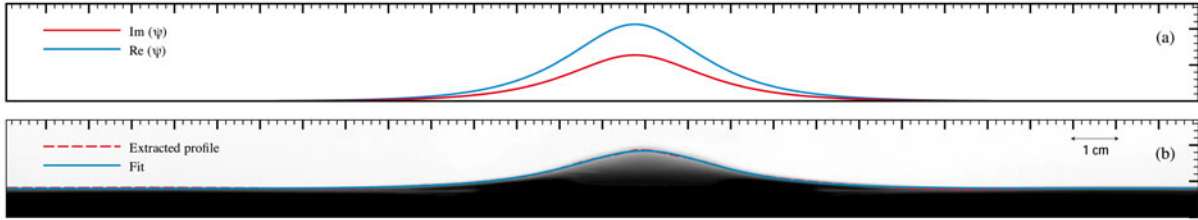


Fig. 8. (Color online) Dissipative soliton in parametrically resonant systems. (a) Stable dissipative soliton observed in the parametrically driven damped nonlinear Schrödinger equation model (3). (b) Snapshot of a non-propagating hydrodynamic soliton observed in a vertically driven 50 cm long and 2.54 cm wide rectangular container, filled with $H = 2$ cm of water. The solid blue and red curve are, respectively, instantaneous surface profile and fit $h(x) = A_s \operatorname{sech}[(x - x_o)/w] + h_0$. Adjusted relevant parameters are $A_s/H = 0.523 \pm 0.001$ and $w/H = 0.786 \pm 0.004$.

driven damped nonlinear Schrödinger equation reads

$$\partial_t R = 2\partial_x R \partial_x \theta + \partial_{xx} R \theta - \mu R + \gamma R \cos(2\theta), \quad (4)$$

$$R \partial_t \theta = -\nu R - R^3 - \partial_{xx} R + R(\partial_x \theta)^2 - \gamma R \sin(2\theta). \quad (5)$$

A non trivial steady homoclinic solution – solutions that connect quiescent state with itself – of the previous model is (dissipative solitons, see [25] and references therein)

$$\cos(2\theta_0) = \frac{\mu}{\gamma}, \quad (6)$$

$$R_{\pm}(x) = \sqrt{2\delta_{\pm}} \operatorname{sech}\left(\sqrt{\delta_{\pm}}[x - x_0]\right), \quad (7)$$

where $\delta_{\pm} \equiv -\nu \pm \sqrt{\gamma^2 - \mu^2} = -\nu - \gamma \sin(2\theta_0)$. The amplitude and width of the dissipative solitons are characterized by $\sqrt{2\delta_{\pm}}$ and $1/\sqrt{\delta_{\pm}}$, respectively. As consequence of the spatial translation symmetry of model (3), the dissipative solitons are a family of states parameterized by a continuous parameter x_0 . This parameter stands for the position of the maximum of the localized state. Figure 8 shows a typical dissipative soliton observed in the parametrically driven damped nonlinear Schrödinger equation and the typical dissipative soliton observed experimentally, which shows a very good agreement with expression (7). Note that the above model has localized states if $\nu < 0$, $\gamma \geq \mu$ and $\gamma^2 < \mu^2 + \nu^2$. In this region, the relation $\cos(2\theta) = \mu/\gamma$ has four solutions in the interval $[-\pi, \pi]$. From this relation, one can infer that the localized states appear or disappear by simultaneous saddle-node bifurcations when $|\gamma| = \mu$. The quiescent state becomes unstable at $\gamma^2 = \mu^2 + \nu^2$, therefore the dissipative soliton becomes unstable at $\gamma^2 = \mu^2 + \nu^2$ with $\nu < 0$. The stable dissipative solitons are characterized by $\text{Re}(\psi)\text{Im}(\psi) > 0$, so both fields are simultaneously positive or negative [25]. Hence, there are two stable dissipative solitons, which are related by the reflection symmetry ($A \rightarrow -A$). These solutions correspond to dissipative solitons in phase or out of phase. From expression (7), one can infer that increasing the forcing amplitude γ , the amplitude and the width of stable dissipative soliton increases and decreases, respectively.

3.2 Effect of basin inclination

As mentioned in section 2.2.4. The inclination of the basin is responsible of inhomogeneous dissipation, injection and detuning (cf. Figs. 5–7). From Figure 7, we can infer that the non-propagating hydrodynamic soliton dissipates less energy in shallow water regions, but changes are small. Direct measurements of energy injection are difficult to realize. However, the local phase measurements (see Fig. 6) show that it does not exhibit significant changes along the channel. Thus, using the relation (5), we conclude that energy injection has a similar spatial behavior to energy dissipation. From the previous statement, considering the formula (7) and the behavior of the soliton amplitude as a function of channel position and detuning, we infer that the detuning has a convex behavior along the channel. In fact, this is a simple consequence of small tilting angles. The local depth can be considered as a function of space: $d(x) = H - x \tan(\phi)$. The correction can be considered as a small perturbation. A Taylor series expansion of ω_o from equation (2) shows that detuning will be a power series of x . The quadratic term turns out to be a good approximation for angles as large as 1° .

To account for these effects in our theoretical description, we consider that detuning, dissipation and injection of energy parameters in parametrically driven damped nonlinear Schrödinger equation become all inhomogeneous, i.e.

$$\begin{aligned} \mu(x) &= \mu + \mu_1(x), \\ \nu(x) &= \nu + \nu_1(x), \\ \gamma(x) &= \gamma + \gamma_1(x). \end{aligned}$$

For small tilt angles, the inhomogeneous terms can be considered as perturbations ($\mu_1(x) \ll 1$, $\gamma_1(x) \ll 1$ and $\nu_1(x) \ll 1$). Hence, equations (4) and (5) read

$$\begin{aligned} \partial_t R &= 2\partial_x R \partial_x \theta + \partial_{xx} R \theta - \mu R + \gamma R \cos(2\theta) \\ &\quad - \mu_1(x)R + \gamma_1(x)R \cos(2\theta), \\ R \partial_t \theta &= -\nu R - R^3 - \partial_{xx} R + R(\partial_x \theta)^2 - \gamma R \sin(2\theta) \\ &\quad - \nu_1(x)R - \gamma_1(x)R \sin(2\theta). \end{aligned} \quad (8)$$

One expects that for small angles, the dissipative solitons are persistent. However, inhomogeneity generates two effects: (i) localized states are modified by the perturbation,

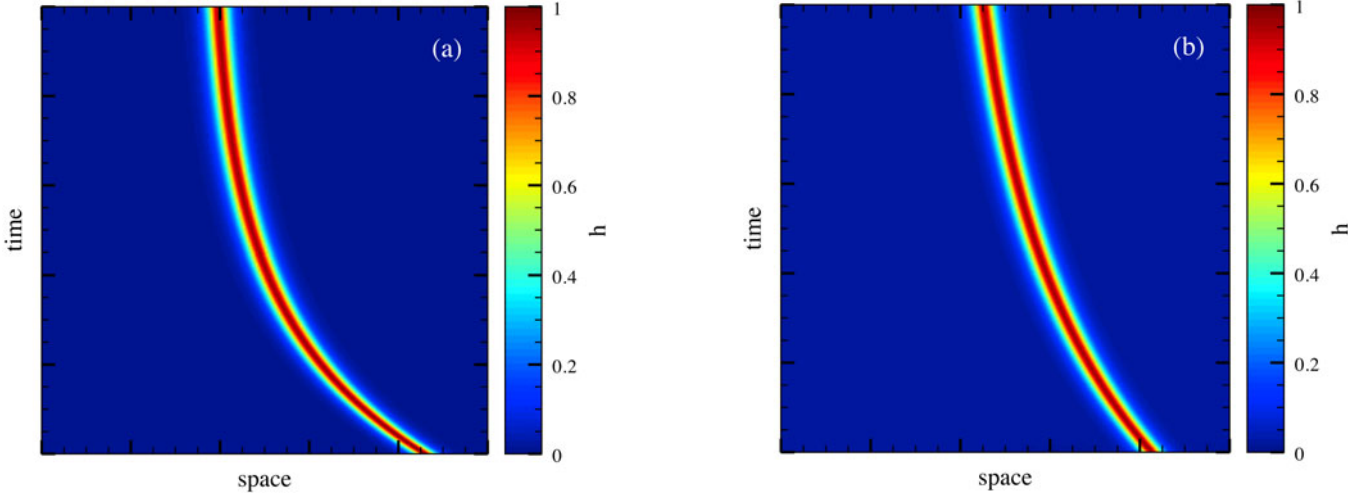


Fig. 9. (Color online) Spatio-temporal diagram of dissipative solitons obtained by numerical simulations of parametrically driven damped nonlinear Schrödinger equation model (3) over 250 points with periodic boundary conditions. The diagrams show 8400 cycles calculated with a time resolution of 1/200 period. (a) $\gamma(x) = 0.40$, $\nu(x) = -0.12 + 0.03x - 0.04x^2$, and $\mu(x) = 0.10$. (b) $\gamma(x) = 0.40$, $\nu(x) = -0.12 + 0.03x - 0.04x^2$, and $\mu(x) = 0.10 - 0.03x + 0.04x^2$.

and (ii) the spatial translational mode of the dissipative solitons – Goldstone mode – acquires a dynamic as a result of the translational symmetry breaking. Motivated by the experimental results, we have considered dissipation, injection and detuning with a quadratic profile along the basin. The space-time diagram of Figure 9 illustrates the typical behavior observed. The soliton propagates into an equilibrium position through a relaxation dynamics – that is, the soliton speed decays systematically until it finds an equilibrium position.

To account for these effects, we consider the following ansatz

$$R(x, t) = R_+(x - x_0(t)) + r(x, x_0),$$

$$\theta(x, t) = \theta_0 + \varphi(x, x_0),$$

where $r(x, x_0)$ and $\varphi(x, x_0)$ are the corrective functions, respectively. Besides, we consider the variable $x_0(t)$ as a slow variable, that is, $\ddot{x}_0 \ll \dot{x}_0 \ll 1$, where $\dot{x}_0(t)$ is the same order of the perturbation. Introducing the above expressions in the set of equations (8) and linearizing the perturbations functions, one finds at leading order

$$\begin{aligned} 2\partial_x\varphi\partial_xR_+ + \partial_{xx}\varphi R_+ &= 2\gamma\varphi\sin(2\theta_0)R_+ + \mu_1(x)R_+ \\ &\quad - \gamma_1(x)\cos(2\theta_0)R_+ - \partial_zR_+\dot{x}_0, \end{aligned} \quad (9)$$

$$\begin{aligned} R_+\partial_t\varphi &= [-\nu - \gamma\sin(2\theta_0) - 3R_+^2 - \partial_{xx}]r \\ &\quad - \nu_1(x)R_+ - 2\gamma R_+\cos(2\theta_0)\varphi \\ &\quad - \gamma_1(x)R_+\sin(2\theta_0), \end{aligned} \quad (10)$$

where $z \equiv x - x_0(t)$ is the coordinate in the co-moving frame. Multiplying equation (9) by the integral factor R_+

and after straightforward calculations, we obtain

$$\begin{aligned} \varphi(x) &= \int^x \frac{dx'}{R_+^2(x')} \int^{x'} dx'' [\mu_1(x'') - \gamma_1(x'')] R_+^2(x') \\ &\quad + \int^x \frac{2\gamma\sin(2\theta_0)dx'}{R_+^2(x')} \int^{x'} dx'' \varphi(x'') R_+^2(x') \\ &\quad - \int^x \frac{\dot{x}_0}{2} dx', \end{aligned} \quad (11)$$

which is a Fredholm integral equation for the field φ [35]. To solve the above integral equation, we consider the limit $\gamma\sin(2\theta_0) = \sqrt{\gamma^2 - \mu^2} \ll 1$, which is equivalent to consider similar injection and dissipation of energy ($\gamma \sim \mu$). Based on this assumption, we can use the approximation

$$\begin{aligned} \varphi &\approx \int^x \frac{dx'}{R_+^2(x')} \int^{x'} dx'' [\mu_1(x'') - \gamma_1(x'')] R_+^2(x') \\ &\quad - \int^x \frac{\dot{x}_0}{2} dx'. \end{aligned} \quad (12)$$

It is important to note that one can iteratively calculate the corrections to the previous approximation in a power series in the small parameter $\sqrt{\gamma^2 - \mu^2}$ [35]. Introducing the linear operator

$$\mathcal{L} \equiv -\nu - \gamma\sin(2\theta_0) - 3R_+^2 - \partial_{xx},$$

equation (10) can be rewritten as

$$\mathcal{L}r = R_+\partial_t\varphi + 2\gamma R_+\cos(2\theta_0)\varphi + \nu_1 R_+. \quad (13)$$

To solve this linear equation, we use the Fredholm alternative [2]. Accordingly, we introduce the following inner product

$$\langle f | g \rangle = \int_{-\infty}^{\infty} f(x)g(x) dx.$$

The linear operator \mathcal{L} is self-adjoint ($\mathcal{L} = \mathcal{L}^\dagger$) under this definition. The kernel of this linear operator – the set of functions $\{v\}$ that satisfy $\mathcal{L}v = 0$ – is of dimension 1. As a result of spatial translation invariance, one has $\mathcal{L}\partial_x R_+ = 0$. Therefore, the field r has a solution if the following condition is satisfied⁵

$$0 = \langle \partial_x R_+ | R_+ \partial_t \varphi + 2\gamma R_+ \cos(2\theta_0) \varphi + \nu_1(x) R_+ \rangle. \quad (14)$$

Using the approximation (12), and considering the dominant terms and after straightforward calculations, yields to

$$\begin{aligned} \dot{x}_0 &= \frac{1}{\int_{-\infty}^{\infty} dx \partial_x R_+^2(x) x} \left[2 \int_{-\infty}^{\infty} dx \partial_x R_+^2(x) \int^x dx' \frac{1}{R_+^2(x')} \right. \\ &\quad \times \int^{x'} dx'' (\mu_1(x'') - \gamma_1(x'')) R_+^2 \\ &\quad \left. + \int_{-\infty}^{\infty} dx \partial_x R_+^2 \cdot \frac{\nu_1(x)}{\mu} \right]. \end{aligned} \quad (15)$$

This expression gives us information of the dynamics of dissipative soliton as a function of spatial disturbance. For small angles and considering the experimental observations, we can consider as a first approximation

$$\begin{aligned} \mu(x) &= \mu + \bar{\mu}_1 x + \bar{\mu}_2 x^2, \\ \gamma(x) &= \gamma + \bar{\gamma}_1 x + \bar{\gamma}_2 x^2, \\ \nu(x) &= \nu + \bar{\nu}_1 x + \bar{\nu}_2 x^2. \end{aligned}$$

The experimental results allow us to infer that the coefficients $\bar{\mu}_2, \bar{\gamma}_2$ are small, and that $\bar{\nu}_2$ is not small. Then, formula (15) can be rewritten

$$\begin{aligned} \dot{x}_0 &= \frac{1}{\int_{-\infty}^{\infty} dx \partial_x R_+^2(x) x} \left[2 \int_{-\infty}^{\infty} dx \partial_x R_+^2 \int^x dx' \frac{1}{R_+^2} \right. \\ &\quad \times \int^{x'} dz (\bar{\mu}_1 - \bar{\gamma}_1) z R_+(z)^2 + \int_{-\infty}^{\infty} dz \partial_z R_+(z)^2 \frac{\bar{\nu}_1}{\gamma} z \\ &\quad + \left\{ 4 \int_{-\infty}^{\infty} dx \partial_x R_+^2 \int^x dx' \frac{1}{R_+^2} \right. \\ &\quad \times \int^{x'} dz (\bar{\mu}_2 - \bar{\gamma}_2) z R_+(z)^2 \\ &\quad \left. \left. + 2 \int_{-\infty}^{\infty} dz \partial_z R_+(z)^2 \cdot \frac{\bar{\nu}_2}{\gamma} z \right\} x_0(t) \right]. \end{aligned} \quad (16)$$

⁵ This is known as the solvability condition or Fredholm alternative.

Consequently, the position of the maximum of the dissipative soliton is ruled by equation (1), where

$$\begin{aligned} \tau^{-1} &= \frac{1}{\int_{-\infty}^{\infty} dx \partial_x R_+^2(x) x} \left[4 \int_{-\infty}^{\infty} dx \partial_x R_+^2 \int^x dx' \frac{1}{R_+^2} \right. \\ &\quad \times \int^{x'} dz (\bar{\mu}_2 - \bar{\gamma}_2) z R_+(z)^2 \\ &\quad \left. + 2 \int_{-\infty}^{\infty} dz \partial_z R_+(z)^2 \frac{\bar{\nu}_2}{\gamma} z x_0(t) \right], \\ P &= \frac{\tau}{\int_{-\infty}^{\infty} dx \partial_x R_+^2(x) x} \left[2 \int_{-\infty}^{\infty} dx \partial_x R_+^2 \int^x dx' \frac{1}{R_+^2} \right. \\ &\quad \times \int^{x'} dz (\bar{\mu}_1 - \bar{\gamma}_1) z R_+(z)^2 + \int_{-\infty}^{\infty} dz \partial_z R_+(z)^2 \frac{\bar{\nu}_1}{\gamma} z \left. \right]. \end{aligned}$$

Therefore, model (1) allows us to capture the dynamics of dissipative solitons observed experimentally in the forced tilted basin with water and numerical simulations of the equation parametrically driven damped nonlinear Schrödinger equation. Figure 9 presents numerical simulation results obtained considering a quadratic dependence on space for both detuning and dissipation. The dynamic evolution shown by these numerical simulations agree very well with experimental results.

It is important to note that when injection and dissipation of energy are of the same order, the system is well described by model (1). However, phase does not exhibit significant corrections in comparison with the maximum amplitude of the soliton. This is consistent with experimental observations.

4 Conclusions

Localized structures are ubiquitous in nature. During the last decade, a constant effort has been focused on the creation mechanisms and features of localized states. Undoubtedly, the next step to boost their potential applications is to advance the manipulation and control of these particle-type solutions. Here, we have presented a theoretical and experimental study of a method of manipulation and control of hydrodynamic solitons in a vertically driven rectangular water basin, based on the tilting of the system.

Experimentally, for a given tilt angle, solitons travel to equilibrium positions through a relaxation process. Long acquisitions are required to observe this behavior, because of the large decay time of the velocity. The equilibrium position depends on the tilt angle, and can be pushed out of the basin if the angle is large enough.

In this system, dissipation, energy injection and detuning are inhomogeneous. Dissipation grows in the direction of depth gradient, but changes are small. Indirect evidence from soliton local phase indicates that energy injections varies less or similarly than dissipation. In contrast, the detuning exhibits a convex behavior along the channel and has shown to have a strong effect on soliton dynamics.

Close to the parametric resonance, the parametrically driven damped nonlinear Schrödinger equation models

this system. The effects of the tilting of the basin are incorporated into this model through space-dependent dissipation, energy injection and detuning. We have deduced an equation for the position of hydrodynamic solitons. This equation is characterized by two terms: a constant speed and a linear relaxation term. The theoretical description reproduces well the hydrodynamic soliton dynamics observed experimentally.

We gratefully acknowledge S. Coulibaly for fruitful discussions. M.G.C. is thankful for the financial support of FONDECYT project 1090045. L.G. thanks the grant support of CONICYT. The authors are also grateful for the fundings of ACT project 127.

References

1. A.C. Newell, *Solitons in Mathematics and Physics* (Society for Industrial and Applied Mathematics, Philadelphia, 1985)
2. See, e.g., L.M. Pismen, *Patterns and Interfaces in Dissipative Dynamics* (Springer Series in Synergetics, Berlin Heidelberg, 2006), and references therein.
3. M. Cross, H. Greenside, *Pattern Formation and Dynamics in Nonequilibrium Systems* (Cambridge University Press, New York, 2009)
4. P. Coullet, Int. J. Bifur. Chaos **12**, 2445 (2002)
5. W. van Saarloos, P.C. Hohenberg, Phys. Rev. Lett. **64**, 749 (1990)
6. P.D. Woods, A.R. Champneys, Physica D **129**, 147 (1999)
7. G.W. Hunt, G.J. Lord, A.R. Champneys, Comput. Methods Appl. Mech. Eng. **170**, 239 (1999)
8. M.G. Clerc, C. Falcon, Physica A **356**, 48 (2005)
9. U. Bortolozzo, M.G. Clerc, C. Falcon, S. Residori, R. Rojas, Phys. Rev. Lett. **96**, 214501 (2006)
10. O. Thual, S. Fauve, J. Phys. (Paris) **49**, 1829 (1988)
11. O. Thual, S. Fauve, Phys. Rev. Lett. **64**, 282 (1990)
12. V. Hakim, Y. Pomeau, Eur. J. Mech. B **S10**, 137 (1991)
13. M. Clerc, P. Coullet, E. Tirapegui, Phys. Rev. Lett. **83**, 3820 (1999)
14. M. Clerc, P. Coullet, E. Tirapegui, Opt. Commun. **167**, 159 (1999)
15. M. Clerc, P. Coullet, E. Tirapegui, Prog. Theor. Phys. **S139**, 337 (2000)
16. M. Clerc, P. Coullet, E. Tirapegui, Int. J. Bifur. Chaos **11**, 591 (2001)
17. M.G. Clerc, P. Encina, E. Tirapegui, Int. J. Bifur. Chaos **18**, 1905 (2008)
18. I.V. Barashenkov, E.V. Zemlyanaya, Phys. Rev. Lett. **83**, 2568 (1999)
19. J.W. Miles, J. Fluid Mech. **148**, 451 (1984)
20. W. Zhang, J. Viñal, Phys. Rev. Lett. **74**, 690 (1995)
21. M.G. Clerc, S. Coulibaly, N. Mujica, R. Navarro, T. Sauma, Phil. Trans. R. Soc. A **367**, 3213 (2009)
22. B. Denardo, B. Galvin, A. Greenfield, A. Larraza, S. Puterman, W. Wright, Phys. Rev. Lett. **68**, 1730 (1992)
23. J.N. Kutz, W.L. Kath, R.D. Li, P. Kumar, Opt. Lett. **18**, 802 (1993)
24. S. Longhi, Phys. Rev. E **53**, 5520 (1996)
25. I.V. Barashenkov, M.M. Bogdan, V.I. Korobov, Europhys. Lett. **15**, 113 (1991)
26. M.G. Clerc, S. Coulibaly, D. Laroze, Phys. Rev. E **77**, 056209 (2008)
27. M.G. Clerc, S. Coulibaly, D. Laroze, Int. J. Bifur. Chaos **19**, 2717 (2009)
28. M.G. Clerc, S. Coulibaly, D. Laroze, Physica D **239**, 72 (2010)
29. N.V. Alexeeva, I.B. Barashenkov, G.P. Tsironis, Phys. Rev. Lett. **84**, 3053 (2000)
30. M.G. Clerc, S. Coulibaly, D. Laroze, Int. J. Bifur. Chaos **19**, 3525 (2009)
31. E. Caboche, F. Pedaci, P. Genevet, S. Barland, M. Giudici, J. Tredicce, G. Tissoni, L.A. Lugiato, Phys. Rev. Lett. **102**, 163901 (2009)
32. J. Wu, R. Keolian, I. Rudnick, Phys. Rev. Lett. **52**, 1421 (1984)
33. J.W. Miles, Proc. Roy. Soc. A **297**, 459 (1967)
34. W. Wei, W. Xinlong, W. Junyi, W. Rongjue, Phys. Lett. A **219**, 74 (1996)
35. G. Arfken, H. Weber, *Mathematical Methods for Physicists* (Elsevier Academic Press, Burlington, 2001).